RSC Advances

PAPER

View Article Online
View Journal | View Issue

Cite this: *RSC Adv.*, 2025, **15**, 22250

Removal of tetracycline antibiotic activity in water by stable cubic phase barium stannate-perovskite nanoparticles under energy-efficient blue light LED irradiation†

Nehal Ashok Waghchoure, Atul Patel, Laxman G. Raikar, Jemi Gandhi, Kampurath Poduvattil Jayadevan * and Halan Prakash *

Photocatalysis is promising for the degradation of antibiotic pollutants in water, which are known to cause the emergence of harmful antibiotic-resistant bacteria (ARB). Importantly, photocatalytic degradation of antibiotic pollutants in water with loss of antibacterial activity in an energy-efficient manner needs to be explored. Here, for the first time, we report degradation of tetracycline (**TC**), a known antibiotic pollutant in water, with removal of its antibiotic activity by cubic-barium stannate ($BaSnO_3$, BSO) perovskite photocatalytic nanoparticles under a blue LED light (367 nm) irradiation, (BSO/LED) system. XRD results revealed a single cubic phase of BSO with a crystallite size of 35 nm. FESEM and TEM images showed that BSO had cubic block-like morphology. BET analysis revealed the mesopores nature of BSO with a surface area of 1.1 $m^2\ g^{-1}$. XPS confirmed the existence of Ba^{+2} and Sn^{+4} ions. The bandgap energy of BSO was determined to be ~3.2 eV. Importantly, photolysis of BSO under blue LED light caused complete degradation of **TC** in water, with a pseudo-first-order rate constant (k_{obs}) value determined as 0.0824 min^{-1}. Radical scavenging and ESR results revealed $O_2^{\cdot -}$ and holes were profoundly generated in the BSO/LED system, causing degradation of **TC** along with antibiotic activity removal. Electrical energy per order (E_{EO}) was determined as 13.63 kWh per m^3 per order, revealing that the BSO/LED system is energy-efficient. Further, BSO was reused four times, highlighting its stability. Degradation byproducts were predicted to be non-toxic by ecological structure activity relationship analysis. Thus, the study discloses an effective photocatalytic degradation of **TC** along with removal of its antibacterial activity that is needed to prevent hazardous ARB, by a stable non-lead-perovskite nano-photocatalyst under an energy-efficient LED source.

Received 26th April 2025
Accepted 23rd June 2025

DOI: 10.1039/d5ra02938d

rsc.li/rsc-advances

1. Introduction

Antibiotics are used to treat infectious diseases in humans and animals.[1–4] However, antibiotic waste leads to the contamination of water bodies.[3] Water contaminated with antibiotics has been reported to cause the emergence of antibiotic-resistant bacteria (ARBs), which can cause severe disease.[5–8] Antibiotics such as tetracycline (**TC**) are highly consumed.[9,10] Importantly, **TC** is not completely metabolised by animals and humans.[11,12] Thus, **TC**s are excreted, and their presence in sewage wastewater has been reported, which is a serious problem for the environment and the health of humans and animals.[13–15] Notably, the presence of **TC**, even in drinking water sources, has been reported.[16] In the aquatic environment, **TC** has a long half-life (34–329 h),[17,18] which could lead to accumulation and cause the spreading of ARBs into the environment.[19] Hence, effective degradation of **TC** in water is urgently needed.

The degradation of antibiotics in water has been reported by various methods such as ozonation,[20] UV photolysis,[21] Fenton/photo-Fenton,[22] and electrochemical process.[23] Photocatalysis is a promising method for the effective degradation of organic micropollutants.[24–26] Photoexcitation of photocatalysts produces excited electron and hole pairs, which are known to generate robust redox reactive species that induce degradation of organic pollutants in water.[27–30] Nanocrystalline perovskites are a class of promising photocatalytic materials.[24,31,32] Earlier, mainly lead-based perovskites, having a formula $MPbO_3$, where M = alkaline earth metals, were reported to show excellent photocatalysis.[33] However, lead-based perovskites have a limitation due to the toxicity of the lead.[34] Hence, the development of non-lead (Pb) based perovskite photocatalysts has gained significant attention. Barium stannate, $BaSnO_3$ (BSO), is emerging as a non-lead (Pb) based perovskite photocatalyst.[35–37] Earlier, the synthesis of BSO photocatalyst has been reported by different methods like

Energy and Environmental Chemistry Laboratory, Department of Chemistry, Birla Institute of Technology and Science, Pilani, K K Birla Goa Campus, Zuarinagar, Goa, 403726, India. E-mail: halanprakash@goa.bits-pilani.ac.in; jayadev@goa.bits-pilani.ac.in

† Electronic supplementary information (ESI) available. See DOI: https://doi.org/10.1039/d5ra02938d

combustion technique,[38] chemical coprecipitation,[39] wet chemicals,[40] sol–gel,[41,42] and hydrothermal.[43] The chemical co-precipitation method has advantages such as low cost, repeatability, high yield, high product purity, and no need of organic solvents.[44] Earlier, photocatalytic degradation of antibiotics in water by modified $BaSnO_3$-based photocatalysts, such as tungsten-modified $BaSnO_3$, heterojunction between $BaSnO_3$ with photocatalysts like TiO_2, copper ferrites and others were reported.,[45–47] Tables S4 and S5.† Importantly, the ability of $BaSnO_3$ nanoparticles to degrade an antibiotic pollutant with the removal of its antibacterial activity after photocatalytic treatment needs to be explored. Moreover, earlier $BaSnO_3$-based photocatalysis were investigated using a conventional xenon lamp.[36] Importantly, a xenon lamp emits wide wavelengths of light in the UV and visible ranges, and appropriate filters are needed for photocatalysis.[48] Thus, a large amount of light is wasted, and xenon lamp sources consume very high power. Notably, bare $BaSnO_3$ has poor light absorption above 400 nm.[49,50] Hence, $BaSnO_3$ photocatalytic activity with light delivered from energy-efficient light sources in the UVA region needs to be explored.[51–53]

It is important to note that light-emitting diodes (LEDs) with UVA light are energy efficient and are emerging as an efficient light source.[54,55] Currently, UVA-LED (367 nm emission maxima), with a wall plug efficiency of 0.046, is commercially available in the market. The wall-plug efficiency of the LED increases as the UVA radiation maximum increases.[56–58] Importantly, the photo excitation of bare $BaSnO_3$ (BSO) photocatalysts under blue light LED (UVA) irradiation for the photocatalytic degradation of antibiotics micropollutants in water, with the elimination of antibiotic activity and reuse of BSO photocatalyst, needs to be evaluated.

Therefore, for the first time, we aimed to study the photocatalytic degradation of antibiotic pollutant **TC** by BSO under blue light LED irradiation (BSO/LED system). A blue LED (367 nm), which closely corresponds to the absorption band of BSO (3.3 eV) was used for irradiation. The BSO obtained by co-precipitation method and characterized by different techniques such as X-ray diffraction spectroscopy (XRD), Field emission scanning electron microscopy (FESEM), transmission electron microscopy (TEM), higher resolution transmission electron microscopy (HR-TEM), Brunauer–Emmett–Teller (BET), selected area electron diffraction (SAED), UV visible spectroscopy, Raman spectroscopy and X-ray photoelectron spectroscopy (XPS). The effect of the initial concentration of **TC** and BSO photocatalyst, the effect of pH, electron spin resonance (ESR), electrochemical analysis, photocatalytic degradation mechanism, degradation byproducts and ecological structure activity relationships (ECOSAR) analysis and antibacterial activity before and after BSO/LED system treatment was presented. The reusability of the BSO photocatalyst was performed and ICP-OES analysed the stability of the BSO photocatalyst. The E_{EO} value for the degradation of **TC** by the BSO/LED system was determined.

2. Experiments

2.1 Materials

The precursor, namely, barium nitrate [$Ba(NO_3)_2$] (98.5% pure, Sigma-Aldrich), stannic chloride [$SnCl_4$] (98% pure, Sigma-Aldrich), sodium hydroxide (NaOH) (Merck), and tetracycline (TCI make) were used in the experiments. The chemicals like methanol, formic acid, and acetonitrile required for HPLC analysis were purchased from Finar Chemicals, and were of HPLC grade. Sodium chloride, sodium bicarbonate, sodium hydrogen phosphate, sulphuric acid, sodium hydroxide, iron(III) nitrate nonahydrate, and humic acid were supplied by Thermo Scientific. The above precursors were directly used without any further purification.

2.2 Synthesis of BSO

The aqueous solution of $Ba(NO_3)_2$ was prepared by dissolving $Ba(NO_3)_2$ in 25 ml distilled water. The solution of $SnCl_4$ was prepared by dissolving $SnCl_4$ in 10 ml of distilled water. The aqueous solution of $SnCl_4$ was added dropwise in the above $Ba(NO_3)_2$ solution, stirring for 1 h. After the formation of the homogenous solution, the aqueous solution of NaOH was added to it and stirred for 30 min. This solution was heated at 70 °C for 3 h with constant stirring until the precipitate was formed. The obtained precipitate was transferred to a Petri dish and dried at 80 °C for another 3 h. This dry residue was crushed using a pestle-mortar, transferred in an alumina crucible, heated to 200 °C in a muffle furnace for 2 h, followed by washing with 15 ml of distilled water, dried for 30 minutes at 80 °C, and then heated for two hours at 200 °C. The purpose of the washing stage was to remove the contaminants such as carbonates, nitrates, salt, and chlorine ions. The above process was repeated three times, and powder was calcined and annealed at 500 °C and 800 °C each for 2 h, respectively and allowed to cool at ambient temperature. The powder thus obtained was further used for the analysis.

2.3 Characterization

XRD measurements (Bruker D8) with Cu Kα radiation ($\lambda = 1.542$ Å) from 20° to 80° with a step size of 0.02 and a step time of 0.6 s. The crystallite size of BSO was calculated to be 35 nm from the Scherrer eqn (1).

$$D = \frac{K\lambda}{\beta\cos\theta} \quad (1)$$

A spectrophotometer (Shimadzu UV-2450) was used to analyse the UV-visible diffuse reflectance spectra (UV-DRS), with $BaSO_4$ as a reference. The measurement range for the spectra was 200–800 nm. The bandgap energy of BSO was calculated from Tauc's eqn (2) and was determined to be 3.2 eV.

$$\alpha h\nu = A(h\nu - E_g)^n. \quad (2)$$

A 532 nm Nd-YAG laser 3.2 mW was used as the laser source for recording Raman spectra (LAB RAM HR Horiba France). The Quanta FEG 250 was used to do FESEM analysis and EDS readings. The voltage for the SEM and EDS experiments was 20 kV. LEICA EM ACE 200 was used for gold sputtering. Transmission Electron Microscopy (TEM) (Fig. 1e) was carried out using FEI Tecnai G2 S-Twin, 200 kV. Thermo Fisher Scientific

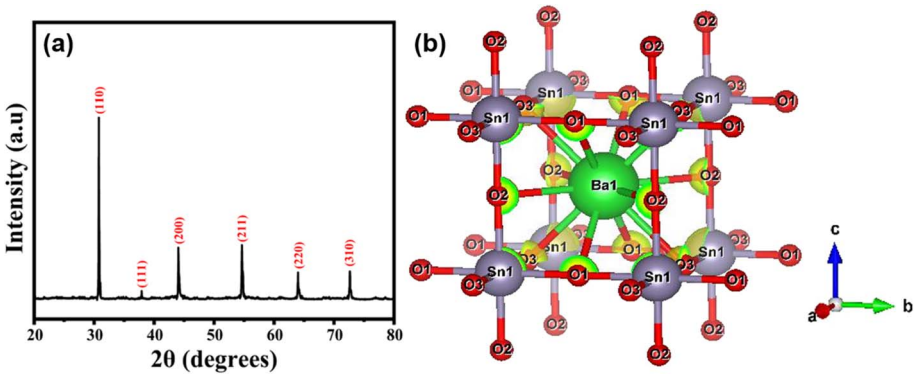

Fig. 1 (a) XRD pattern of single phase BSO synthesised by co-precipitation method, (b) crystal structure of BSO. The centre ball is Ba, and small (red) balls on the edge are the oxygen atoms, and the Sn (violet), which forms an octahedron, is shown coordinating with six oxygen atoms.

(UK) K-Alpha X-ray Photoelectron Spectrometer was used to conduct X-ray photoelectron spectroscopy (XPS).

Electron Spin Resonance (ESR) was recorded using a JEOL ESR Spectrometer. Spin-trapping agents, including DMPO, TEMP, and TEMPO, were used for the analysis. The conditions employed were magnetic centre field = 336 mT, microwave power = 0.995 mW, and microwave frequency of 9.440 GHz. Samples were taken out and examined at the proper intervals.

A BioLogic SP-150e electrochemical workstation was used to carry out the electrochemical analysis. The Mott–Schottky was plotted using electrochemical impedance spectroscopy (EIS) and chronoamperometric measurements, which were performed using a three-electrode electrochemical cell. The Mott–Schottky plots were plotted using EIS measurements, with a reference electrode (Ag/AgCl) having a potential between −2.0 V and −0.4 V with a frequency range of 100 kHz to 10 Hz. The BSO was prepared in ethanol as the working electrode with Nafion acting as a binder. After that, it was applied to a 1 cm^2 region on fluorine-doped tin oxide (FTO) glass slides. The reference electrode was Ag/AgCl (saturated KCl), while the counter electrode was graphite. For each photoelectrochemical experiment, 15 ml of 0.1 M Na_2SO_4 electrolyte solution, pH = 5.8 and an LED light source (367 nm) were used.

2.4 Photocatalytic degradation experiments

Deionised water was used in the overall photocatalytic experiments. A photocatalytic degradation experiment was conducted in an 80 ml quartz glass reactor at room temperature (25 °C). A desirable amount of **TC** and BSO were mixed, and the solution was stirred for 30 minutes in the dark. After reaching adsorption equilibrium, 500 µl of the solution was taken in a microcentrifuge tube, which was captioned as 0 min reading and was later centrifuged, and supernatant was used for the analysis. The LED light was switched on and the samples were collected at a specific time interval. An ultraviolet-A light-emitting diode (UVA LED) with a maximum wavelength (λ_{max}) of 367 nm was used for the degradation experiment. The irradiance spectra of 367 nm LED light is shown in Fig. S5.† The distance between the LED light and the quartz was 0.5 cm, and an external fan was used to keep the LEDs cool. The solution was stirred continuously throughout the experiment, and 0.5 ml solution was withdrawn at a 3 min time interval in a 1 ml microcentrifuge tube containing 10 µl of methanol as a quencher. This solution was centrifuged at 5000 rpm for 10 min, and the supernatant solution was analysed using high-performance liquid chromatography (HPLC Shimadzu technologies). The Phenomenex Kinetex EVO C18 2.6 µm, 4.6 × 100 mm column was used for HPLC. An isocratic technique was used with a mobile phase of acetonitrile and formic acid (0.1%) in water (10 : 90) at a flow rate of 0.8 ml min^{-1}. The limit of detection was found to be 0.0944 µg L^{-1} for **TC** with an R-square value of 0.999 (Fig. S1†).

The following eqn (4) and (5) were used to compute the photocatalytic degradation efficiency (φ).

$$\varphi = \frac{C_0 - C_t \times 100}{C_0} \quad (3)$$

$$-\ln\left(\frac{C_0}{C_t}\right) = kt \quad (4)$$

To analyse the dynamics data, the first-order model was used:

Where φ is the degradation efficiency, C_0 (mg L^{-1}) and C_t (mg L^{-1}) are the concentrations at the initial and final (after t min), and k is the first order rate constant (min^{-1}). The chemical oxygen demand (COD) was performed to analyse the organic content after the degradation of **TC**. Initially, the COD before degradation was 9 mg L^{-1}, which was reduced to 4 mg L^{-1} with an equilibrium time of 45 min for 80 ml **TC** solution with 0.4 g L^{-1} of BSO catalyst. The reusability of the BSO catalyst was performed by centrifugation and reuse.

A scavenging experiment was performed using isopropyl alcohol (IPA) as a $HO^{\bullet}$ radical scavenger, sodium azide (NaN_3) as a $^1O_2$ scavenger, ethylenediamine tetra acetic acid (EDTA) as a hole (h^+) scavenger, and 1,4-benzoquinone (BQ) as a superoxide radical anion ($O_2^{\bullet -}$) scavengers. Spin-trapping agents such as TEMP in water and DMPO in water were employed for the analysis of singlet oxygen, and $HO^{\bullet}$, respectively. BSO and DMPO in methanol was used to identify $O_2^{\bullet -}$ radical.[59] The aqueous BSO and TEMPO were used to detect holes (h^+).

2.5 Toxicity assessment

2.5.1 ECOSAR. Acute and chronic ecotoxicity of **TC** and its intermediate products was predicted by the Ecological Structure–Activity Relationship (ECOSAR application 2.2) developed by USEPA for green algae, fish, and daphnids.[60–62] The toxicity prediction of organic chemicals is based on available data by structure–activity relationships (SARs). The Globally Harmonized System of Classification and Labelling of Chemicals was used for the categorization of toxicity levels, as shown in Fig. 14.

2.5.2 Antibacterial activity. Antibacterial activity of **TC** (10 mg L^{-1}) before and after treatment by BSO/LED system was assessed by the agar well diffusion method (Clinical and Laboratory Standards Institute, CLSI) as per standard protocol.[63] The antibacterial activity of **TC** was tested against Gram-positive *Enterococcus faecalis* and Gram-negative *Escherichia coli*. The plates had a final depth of 4 mm after being created in 90 mm sterile Petri dishes with 22 ml of nutrient agar. The spread-plate technique was used to apply 0.1 ml of the tested bacteria's inoculum suspension to the solid media plates. A sterile well borer was used to punched round wells (9 mm in diameter) into agar plates. 100 μl of samples were filled in the wells. The plates were incubated for 24 h at 37 °C, and the zone of inhibition around the well was measured (mm). Experiments were repeated thrice.[60]

2.6 Electrical energy determination

The electrical energy order (E_{EO}) was calculated to find the electrical energy required to degrade the contaminant in a water unit. It was calculated as discussed below

$$E_{EO} = \frac{P \times t \times 1000}{V \times 60 \times \log \frac{C_i}{C_f}} \quad (5)$$

$$\left(\ln \frac{C_i}{C_f}\right) = k' \times t \quad (6)$$

where P is the power (kW) to drive the LEDs, t is the irradiation time (min), V is the volume (litre), C_i and C_f are the initial and final concentration of **TC** and k' is the pseudo-first-order rate constant (min^{-1}) for the decay of **TC** degradation.[64] The UVA LED had an electrical input power rating of 2.34 W (12 V and 195 mA, with E_{max} = 367 nm and FWHM = 15 nm).

From eqn (5) and (6) E_{EO} can be modified into

$$E_{EO} = \frac{38.4 \times P}{V \times k'} \quad (7)$$

Using the above formula, the E_{EO} of the LEDs was calculated as 13.63 kWh per m^3 per order.

3. Results and discussion

3.1 Characterization of BSO

3.1.1 XRD analysis. The XRD diffraction peaks centred at 30.68°,37.80°, 43.93°, 54.53°, 63.87°, and 72.54° corresponds to the planes of (1 1 0), (1 1 1), (2 0 0), (2 1 1), (2 2 0), and (3 1 0) of the cubic phase of BSO (JCPDS 15-0780), (Fig. 1a).[65] The lattice constant for the cubic BSO was calculated as 4.117 Å. The *d*-spacing for the intense peak of the 110 planes at 30.68° was calculated to be 0.2910 nm, which matches the JCPDS file 15-

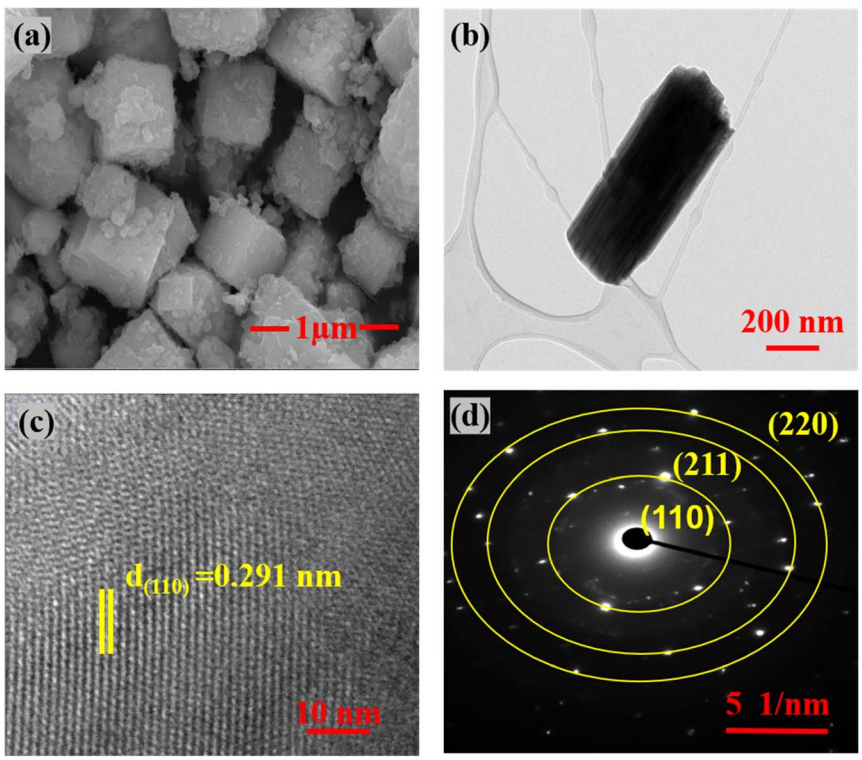

Fig. 2 (a) FE-SEM image of BSO with cubic morphology, (b) TEM image of BSO, (c) HRTEM with *d*-spacing 0.29 nm, and (d) SAED image of BSO.

0780. The crystal structure of BSO is made using VESTA software[66] that depicts the positions of all the atoms is shown in Fig. 1b. The crystallite size of BSO was determined to be 35 nm from the Scherrer eqn (1).

3.1.2 FESEM and TEM analysis. FESEM images revealed the block-like morphology of BSO (Fig. 2a). It was observed that the formed cubes are well separated from each other. These cubes are formed *via* the process of Ostwald ripening.[65] These nanocrystals aggregate to form cubic particles (~1 μm). These cubic particles have rough surfaces. The selected area of the FESEM image and its EDS data are shown in Fig S3a and b,† respectively. A TEM analysis of BSO revealed the nanosheet-like structures that were aggregated to form a block-like morphology (Fig. 2b). The HRTEM image for BSO shows the inter-planar spacing of 0.291 nm, attributed to the lattice plane of 110 (Fig. 2c). This value matches the *d*-spacing value calculated through the XRD peaks for the 110 planes observed at 30.68°. SAED image of BSO (Fig. 2d) shows the polycrystalline nature of the prepared BSO sample. The bright spots in the SAED image were attributed to the 110 planes corresponding to the most intense peak in XRD.[67]

3.1.3 Raman, surface area analysis, and absorption property. Two strong bands were observed at 129.2 cm^{-1} and 147.1 cm^{-1}. Importantly, these peaks correspond to the symmetric bending mode (v_5F_{2g}) of [SnO_6] octahedral unit.[68,69] Further, the peak at 212.8 cm^{-1} was assigned to the asymmetric bending mode (v_4F_{1u}).[70] The bands at 540.3 cm^{-1} and 639.1 cm^{-1} were assigned to the Raman active asymmetric stretching mode (v_2E_g) and symmetrically stretching (v_1A_{1g}) of the Sn–O bond,[71] respectively (Fig. 3a). The Ba–O bond peak occurred at 408.9 cm^{-1}.

The nitrogen adsorption–desorption isotherm of BSO corresponds to a type IV isotherm with an H4 type of hysteresis loop, revealing mesoporous material with narrow-slit pores, as per the IUPAC categorisation of hysteresis loops.[72] The surface area, total pore volume, and pore diameter (BJH) were calculated to be 1.10 $m^2\ g^{-1}$, 0.0031 $cm^3\ g^{-1}$, and 3.16 nm, respectively, (Fig. 3b and c).[73,74] The surface area obtained in the present work was slightly lower compared to the earlier suggested report, where $BaSnO_3$ was obtained *via* microwave-assisted hydrothermal treatment.[75] Importantly, the Tauc plot reveals that BSO has an absorption band edge/tail around 390 nm, and the bandgap energy (E_g) of BSO was calculated to be around 3.2 eV (Fig. 3d).[76]

3.1.4 XPS, Mott–Schottky, and band alignment. Fig. 4a shows the XPS survey of BSO, revealing the presence of Ba, Sn,

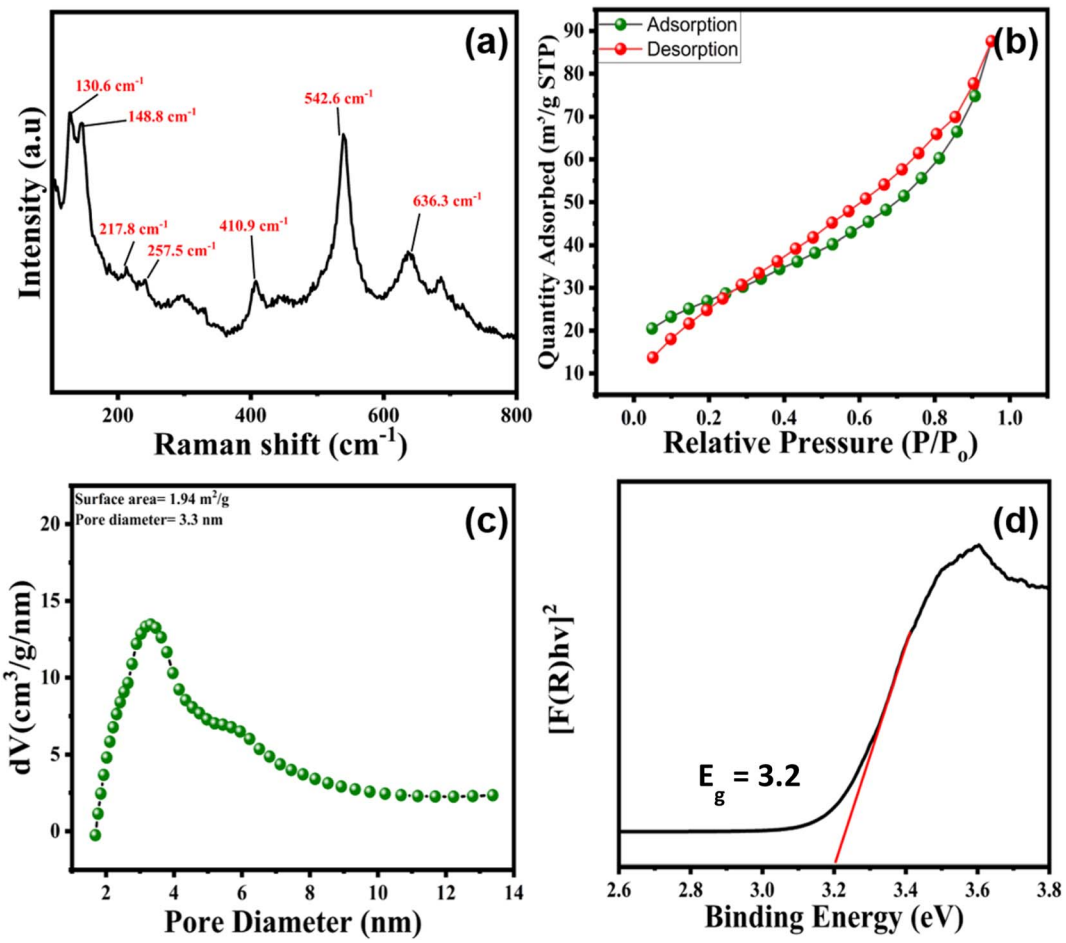

Fig. 3 (a) Raman spectra of pure BSO, (b) nitrogen adsorption–desorption isotherms, (c) BJH pore-size distributions of BSO, and (d) Tauc plot to determine the bandgap of BSO. Minor tick in Fig. 3d.

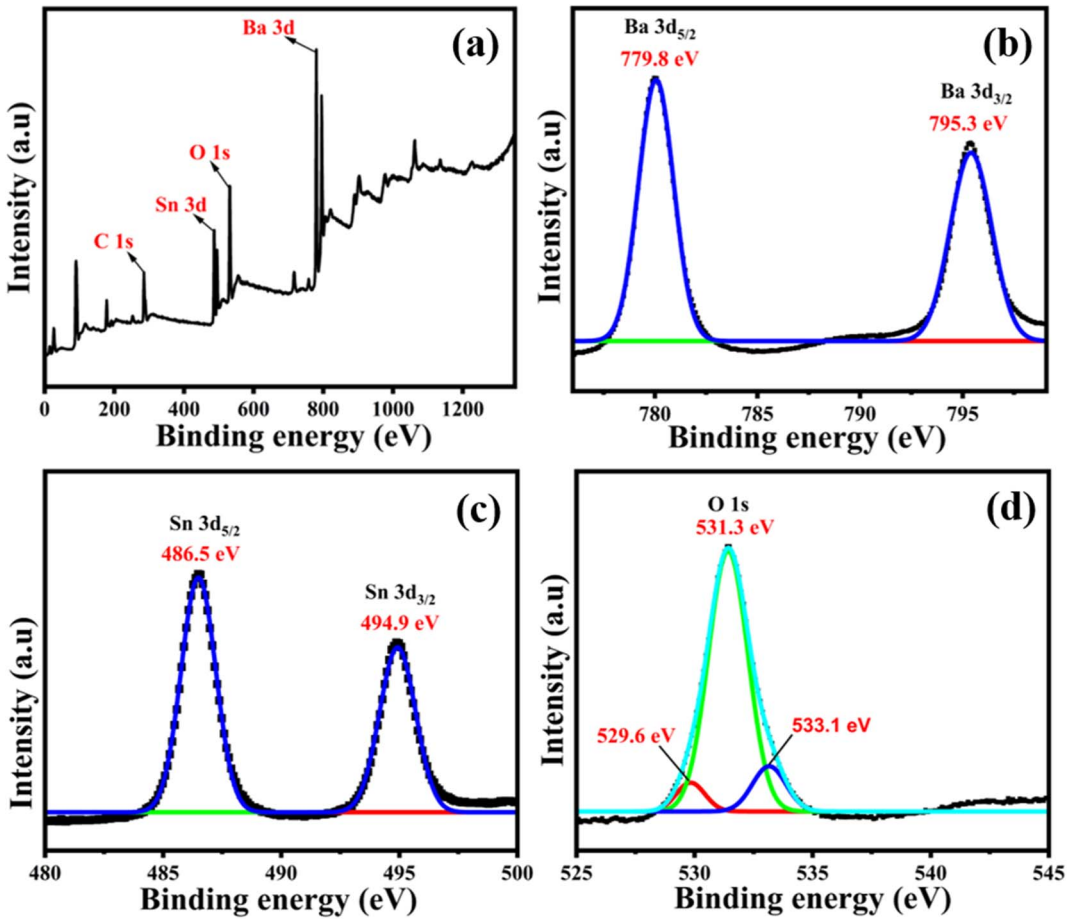

Fig. 4 XPS of bare BSO, (a) XPS survey of BSO, (b) the core-level splitting of peaks of Ba, (c) the core-level splitting of peaks of Sn, and (d) the core-level splitting of peaks of O.

and O. The presence of the carbon (C) peak in the XPS survey is attributed to the adventitious carbon from the sample holder.[77] The Ba 3d XPS spectrum showed two peaks at 779.8 eV and 795.3 eV (Fig. 4b). The difference between two peaks is 15.5 eV, which confirms Ba is having Ba^{2+} oxidation state in BSO.[78] In Fig. 4c, the Sn 3d XPS spectrum showed two peaks at 486.5 eV and 494.9 eV. The difference between two peaks is 8.4 eV, which confirms Sn is exist in Sn^{4+} oxidation state.[79] O 1s XPS spectrum showed three deconvoluted O 1s peaks at 529.6 eV, 531.3 eV, and 533.1 eV, which were attributed to lattice oxygen, adsorbed oxygen species in the oxygen-deficient region, and adsorbed hydroxy species, respectively (Fig. 4d).[80,81] These results confirm the presence of Ba, Sn, and O elements in BSO.

Further, the energy difference between the Fermi level and the valence band (E_d) was determined to be about 2.56 V from the XPS valence band spectrum of BSO, Fig. 5a. The Fermi level

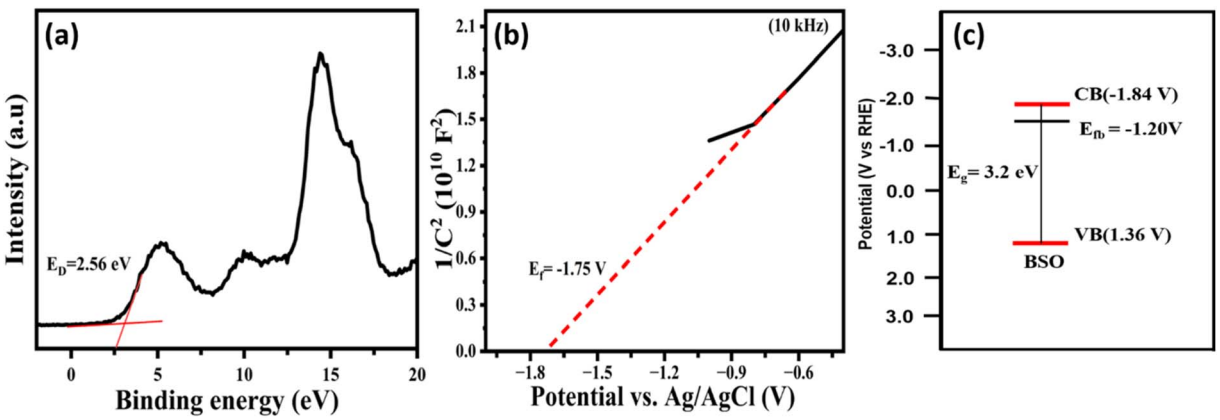

Fig. 5 (a) XPS valence band spectra, (b) Mott Schottky plot of BSO, (c) band alignment of BSO.

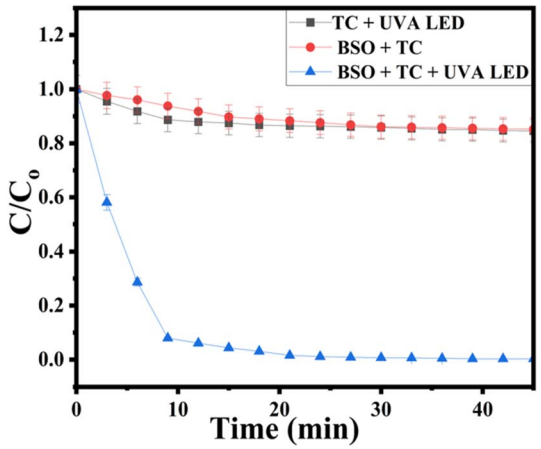

Fig. 6 Degradation of TC by BSO under UVA-LED irradiation. TC = 10 mg L^{-1}, BSO = 0.4 g L^{-1}.

(flat band potential E_f) was determined to be −1.75 V (*vs.* Ag/AgCl) from the Mott–Schottky plot (Fig. 5b), and corresponding E_f value was − 1.20 V (*vs.* NHE). Thus, the position of the valence band was determined to be 1.36 V (*vs.* NHE), based on the eqn ($V_b = E_d + E_f$).[82] Further, the position of the conduction band was determined to be −1.84 V (*vs.* NHE) based on the equation $E_{CB} = E_{VB} - E_g$, where E_g is the band gap energy. The band structure of BSO highlighting the position of VB, CB, and E_f is presented in Fig. 5c. A light-emitting diode (LED) that has an emission profile (Fig. S3,† λ_{max} = 367 nm, 3.3 eV), and strongly overlaps with the absorption (band gap energy of 3.2 eV) of the BSO, was used to evaluate the ability of the BSO photocatalyst (BSO/LED) system to degrade organic pollutant, as discussed below.

3.2 Photocatalysis

3.2.1 Degradation TC by BSO/LED system. BSO/LED photocatalytic system caused 98.42% degradation of **TC** within 45 min as shown in Fig. 6. Notably, the degradation of **TC** by UVA light alone and by BSO alone was not effective in comparison to BSO/LED system. Hence, these results revealed that adsorption plays no significant role in **TC** removal, whereas photocatalysis, due to the excitation by the UVA light irradiation, caused the degradation. Excitation of the bandgap of BSO (3.2 eV) with LED causes the generation of electron and hole pairs that are known to initiate the photocatalytic degradation of organic pollutants. Additionally, the degradation of **TC** under 400 nm LED light with similar irradiance values was also performed and the results showed a reduction in degradation efficiency, with 93.23% degradation achieved in 45 minutes. The higher efficiency observed under 367 nm light (98.42%) is attributed to its better photon energy and stronger absorption by the photocatalyst, leading to enhanced generation of reactive species (Fig. S6†). Further, the effect of BSO concentration, initial concentration of antibiotic pollutant **TC**, pH effect, and elucidation of the photocatalytic mechanism were investigated, as discussed below.

3.2.2 Effect of concentration of TC on the degradation rate. The rate of degradation decreased with an increase in the initial concentration of **TC** (Fig. 7a). The pseudo-first-order rate constant values, k_{obs}, (Table S3†) were summarised. The k_{obs} values gradually decreased with the increase in the initial concentration of **TC** (Fig. 7b). This result was attributed to the inner filter effect. The inner filter effect refers to the maximum absorption of light at a relatively higher concentration of **TC**, which reduces the transmittance of light and prevents the absorption of light and photoexcitation of the BSO.[83,84] Hence, at the comparatively higher concentrations of **TC**, the reactive radical species involved in the oxidation are not sufficiently available, thereby reducing the degradation efficiency.[85,86]

3.2.3 Effect of BSO dosage on the degradation of TC. The **TC** degradation efficiency was gradually increased with an increase in BSO dosage from 0.1 g L^{-1} to 0.4 g L^{-1}, and further increasing the dosage of BSO slightly retarded the rate, exhibiting a bell shape trend Fig. 8b. The results revealed 0.4 g per L dosage had maximum k_{obs} value, and it was considered to be the optimal BSO dosage for the photocatalytic experiments.[87] The effect of BSO catalyst dosage (0.1 g L^{-1} to 0.6 g L^{-1}) on tetracycline (**TC**) degradation was investigated (Fig. 8a).

3.2.4 Effect of pH on the degradation of TC by BSO/LED system. pH of the water is known to influence the surface

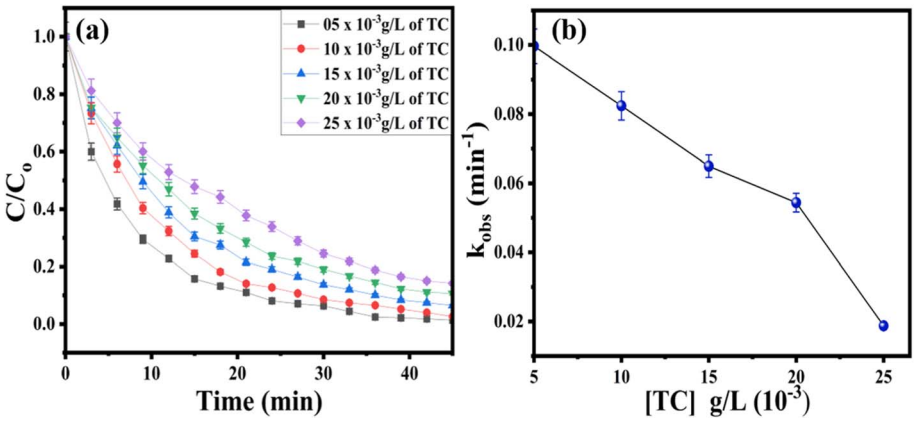

Fig. 7 (a) Effect of TC dosage on degradation rate, and (b) k_{obs} *vs.* TC g L^{-1}. TC = 10 mg L^{-1}, BSO = 0.4 g L^{-1}.

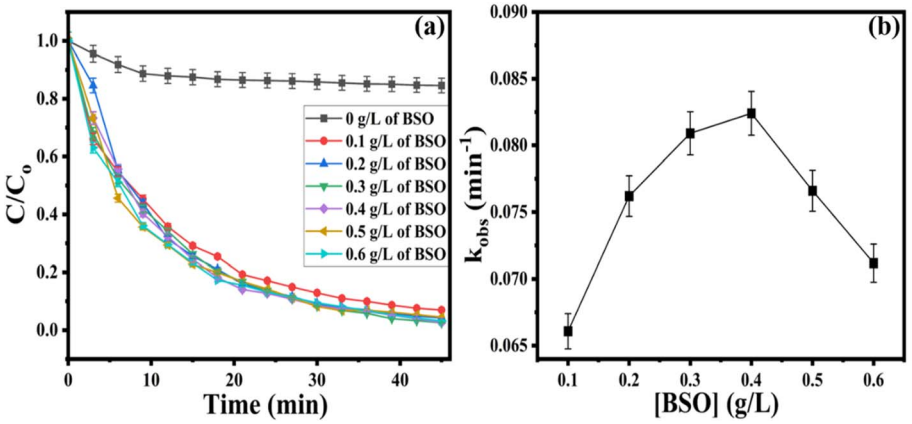

Fig. 8 (a) Effect of BSO dosage on TC degradation, and (b) k_{obs} *vs.* concentrations of BSO (g L^{-1}). TC = 10 mg L^{-1}, BSO = 0.4 g L^{-1}.

charge of photocatalyst and pollutant, and therefore, the rate of photocatalysis depends on the pH. The k_{obs} values for degradation of **TC** by BSO/LED system at pH 5 and 6.5 were found to be almost similar, and at pH 9 and 11, there was a slight reduction (Fig. 9a and b). However, at a highly acidic pH 3, there was no significant degradation of **TC** (Fig. 9a). At a highly acidic pH 3, the zeta potential of BSO is positive, *i.e.*, 9.3 (Fig. S7†). Further, at pH 3 and below, the **TC** is in protonated form.[88] Hence, there is a repulsion between the positively charged photocatalyst, BSO and positively **TC** molecule at pH 3 (and below), thereby, the degradation is retarded compared to other higher pH of the solution Fig. 9. At pH 5, the zeta potential of BSO is negative. In contrast, the **TC** molecules are in protonated form, leading to electrostatic attraction between the BSO and **TC**, and favours photocatalytic degradation compared to pH 3. At alkaline pH 9 and 11, the catalytic surface and the **TC** molecules acquire negative charges (anionic forms). Thus, catalysts and **TC** molecules repulsion may cause reduction of the k_{obs} values, in comparison to pH 5 and near neutral pH 7.7.

Interestingly, at highly alkaline pH, the degradation was not significantly reduced compared to acidic conditions at pH 3. This result indicates that the positively charged holes may significantly attract the negatively charged **TC** molecule under alkaline conditions and cause appreciable degradation, Fig. 9b. Overall, these results reveal that the BSO/LED system has good degradation ability over a wide pH range.[89]

3.2.5 Effect of inorganic ions and different water matrix on the degradation of TC. Fig. 10a illustrates the effect of tap water and simulated groundwater on **TC** degradation by BSO/LED system. **TC** degradation efficiencies in the tap and simulated groundwater were determined to be 63.7% and 46.7%, respectively, compared to 98.42% in Milli-Q water (control), within 45 min. This decline in degradation efficiency is likely due to the presence of inorganic ions and natural organic matter in tap water and simulated groundwater[90] (Tables S1 and S2†) that interact with reactive species produced during photocatalysis, thereby hindering **TC** degradation. Additionally, the BSO/LED system effectively degraded **TC** at lower initial concentrations (200 μg L^{-1} to 1 mg L^{-1}), Fig. S8.† These results suggest that the BSO/LED system is an effective treatment for the degradation of **TC** pollutants at environmentally relevant concentrations. Earlier, **TC** pollutant was reported to be in the range of ng L^{-1} to μg L^{-1} (environmentally relevant concentration) in river and drinking water sources.[91]

Further, the effect of common inorganic anions in water, *viz.*, Cl^-, NO_3^-, HCO_3^-, SO_4^{2-}, and PO_4^{2-} and the effect of organic matter (humic acid, HA) on the degradation of **TC** by the BSO/LED system was explored. Fig. 10b shows the impact of the

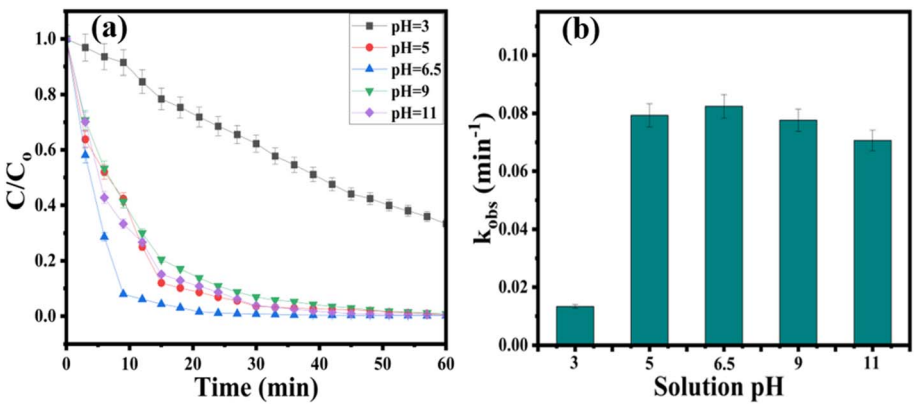

Fig. 9 (a) Effect of initial pH on tetracycline degradation, and (b) k_{obs} *vs.* pH; [TC] = 10 mg L^{-1}, [BSO] = 0.4 g L^{-1}.

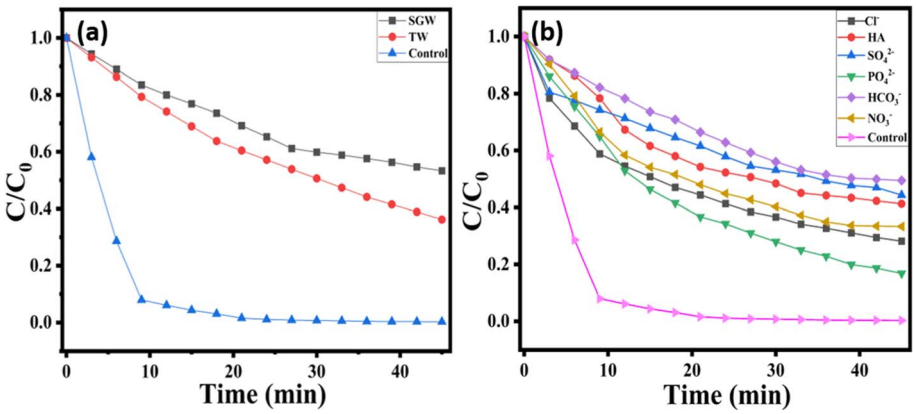

Fig. 10 (a) Effect of water matrices on TC photo-degradation performance by BSO/LED system (b) effects of co-existing inorganic ions and HA and, experimental conditions: [TC] = 10 mg L^{-1}, BSO = 0.4 g L^{-1}, volume: 80 ml, [ion] = 10 mM. SGW = simulated groundwater, TW = Tap water.

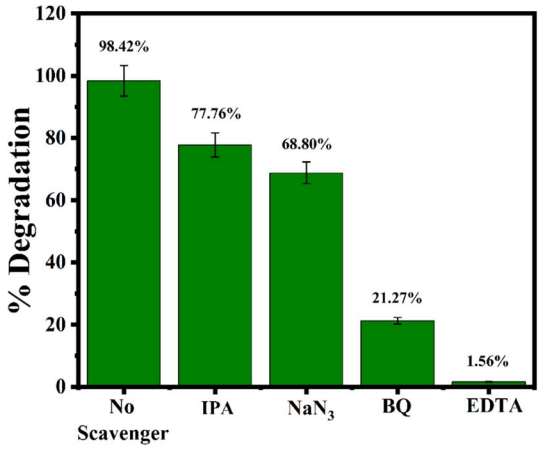

Fig. 11 The effect of scavenging agents on the degradation TC [IPA] = [NaN_3] = [BQ] = [EDTA] = 100 mM. [TC] = 10 mg L^{-1}, BSO = 0.4 g L^{-1}.

inorganic ions on the **TC** degradation efficiency. Among the anions, HCO_3^- exhibits a significant inhibition for the degradation of **TC**, possibly due to the effective scavenging of HCO_3^- by the h^+, resulting in decreased photocatalytic activity. Other anions *viz* Cl^-, NO_3^- and PO_4^{2-}, may undergo scavenging reactions leading to secondary reactions that produce less reactive species as shown in the reaction eqn (8)–(12) mentioned below.[29,92,93]

$$HCO_3^- + h^+ \rightarrow CO_3^{\bullet -} \quad (8)$$

$$Cl^- + h^+ \rightarrow Cl^{\bullet} \quad (9)$$

$$Cl^{\bullet} + Cl^- \rightarrow Cl_2^{\bullet -} \quad (10)$$

$$NO_3^- + h^+ \rightarrow NO_3^{\bullet} \quad (11)$$

$$HPO_4^{2-} + h^+ \rightarrow HPO_4^{\bullet -} + h^+ \quad (12)$$

Moreover, humic acid (HA), a natural organic compound frequently detected in aquatic environments, significantly impacts the degradation of the tetracycline (**TC**) BSO/LED system. HA inhibits the degradation process by several mechanisms. Firstly, HA can adsorb onto the photocatalyst's surface, obstructing its active sites and hindering catalytic activity. Additionally, HA exhibits strong absorption in the UVA region, resulting in an inner filter effect that reduces the penetration of UVA light and limits photon availability for photocatalysis. Moreover, HA may react with reactive species generated in the reaction system, reducing the efficiency of **TC** degradation.[94]

3.2.6 Photocatalytic degradation mechanism. The degradation of **TC** by the BSO/LED system in the presence of isopropyl alcohol (IPA), sodium azide (NaN_3), benzoquinone (BQ), and EDTA were summarised in Fig. 11. IPA, NaN_3, BQ, and EDTA are known to scavenge $HO^{\bullet}$, $^1O_2$, $O_2^{\bullet -}$, and h^+, respectively. Importantly, EDTA had the highest inhibiting effect compared to other scavengers. Based on these results, the scavenging order was as follows: EDTA > BQ > NaN_3 > IPA. Thus, hole (h^+) is the predominant species for the degradation of **TC**, followed by $O_2^{\bullet -}$, whereas $HO^{\bullet}$ and $^1O_2$ had a minimum effect. Hence, the proposed BSO/LED system effectively generates reactive species, *viz.*, superoxide and hole for photocatalytic degradation of **TC**.[95]

ESR was utilized to identify the radicals generated during the photocatalysis. As illustrated in Fig. 12a, the DMPO-superoxide adduct was observed clearly in the BSO/LED system. The oxidation of TEMPO by h^+, causing a decrease in TEMPO signal, was observed. Further, the photocatalysis reaction in the presence of DMPO showed no noticeable signals of DMPO–OH adduct, revealing $HO^{\bullet}$ radical was not effectively generated in BSO photocatalysis Fig. 12b. Additionally, TEMP-singlet oxygen adduct single was not appreciably formed under BSO/LED system.[96,97] Fig. 12c. These results corroborate the radical scavenging results, holes, and superoxide radical for the degradation of **TC**.[29,82]

TC under UVA LED irradiation showed no significant degradation (14.2%) because the energy gap between the HOMO and LUMO of **TC** is 4.2 eV,[98] which is too high for a UVA LED (3.3 eV) to induce direct photochemical excitation and reaction. **TC** was also not effectively removed by adsorption onto the BSO (Fig. 6). However, 98.42% degradation efficiency was

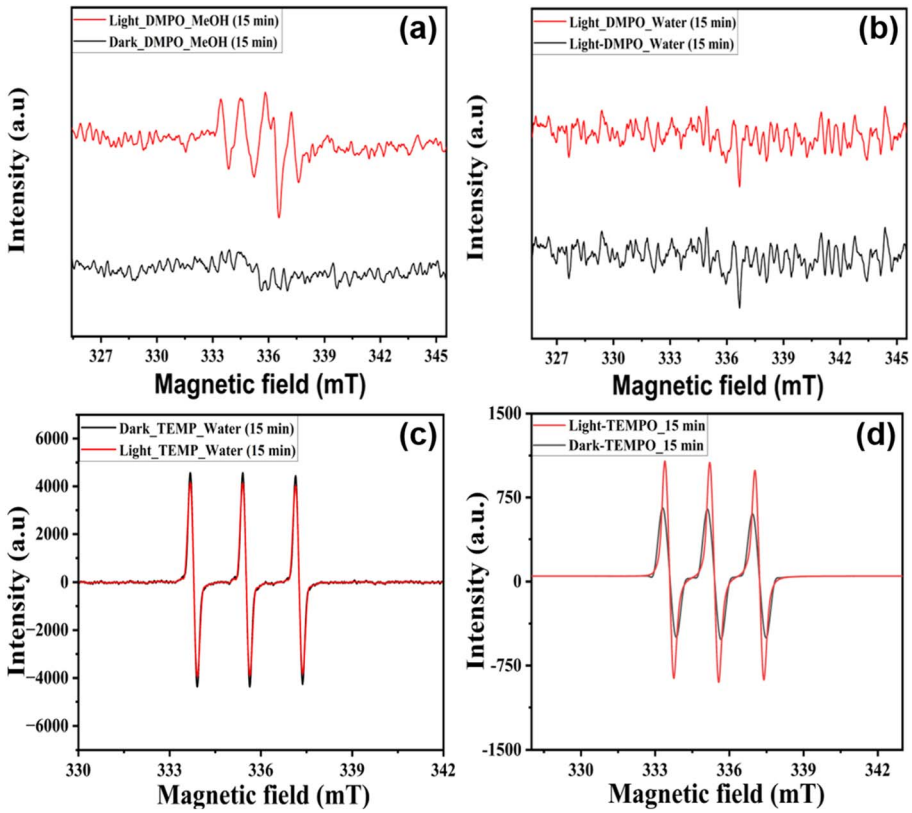

Fig. 12 ESR spectra of (a) DMPO–$O_2^{\cdot-}$ in methanol, (b) DMPO–$HO^{\bullet}$ in water, (c) TEMP–$^1O_2$ in water, and (d) TEMPO–h^+ in water for the dark, and light experiment. ([DMPO] = [TEMP] = 30 mM, BSO = 0.4 g L^{-1}).

achieved by the BSO/LED system within 45 min. Based on the above results, the BSO/LED system photocatalysis mechanism is proposed as discussed below. BSO, upon light irradiation, generates e^- and h^+ pairs. A clear photocurrent response was observed for the BSO under LED irradiation, Fig. S9.† Interestingly, in the presence of **TC**, the photocurrent response was significantly enhanced, revealing that holes generated in under irradiation were scavenged by the **TC**. The Nyquist plot (Fig. S10a†) and Bode's plot (Fig. S10b†) were obtained, and the f_{max} (84.64) value was obtained from the Bode plot. The free charge carrier lifetime was determined to be 1.18 ms using eqn (13).[99]

$$\tau = \frac{1}{2\pi f_{max}} \quad (13)$$

This result further corroborates with the effect of pH, scavenging by the EDTA, and the effect of bicarbonate ion, emphasising that the holes play a pivotal role in degradation next to the superoxide radical ion. The position of the conduction band (CB) −1.84 V (RHE) reveals that BSO is thermodynamically favourable to reducing the oxygen to a superoxide radical anion. Superoxide radical anion is known to induce the oxidation of antibiotic pollutants.[29] The E_{CB} value has more negative potential (*i.e.*, −1.84 V) than the standard redox potential of $O_2^{\cdot-}$ ($E(O_2/O_2^{\cdot-}) = -0.33$ V), which is favourable for formation of superoxide radicals ($O_2^{\cdot-}$) by the reaction between O_2 and excited photoelectron in CB.[100] E_{VB} is 1.36 V which is less compared to the standard potential of $HO^{\bullet}$ ($E(HO^-/HO^{\bullet}) = +1.99$ V, and $E(H_2O/HO^{\bullet}) = +2.73$ V), and hence the formation of hydroxy radical ($HO^{\bullet}$) is not favourable, and corroborate well with the ESR, and radical scavenging experiments.[101,102] The position of the valence band (VB) at 1.36 V reveals BSO is not efficient in producing hydroxyl radicals by oxidation of the water molecule. Thus, hydroxyl radicals were not observed in the ESR, and in the presence of hydroxyl radical scavenger, the photocatalysis was not retarded significantly. Under acidic conditions, pH = 3, the $O_2^{\cdot-}$ may also go undergo reaction with photogenerated h^+ to form less reactive H_2O_2 which may also contribute to retard the degradation reaction, in addition to electrostatic repulsion between positively charged **TC**, and BSO as discussed earlier.[103] The degradation mechanism of **TC** by using BSO/LED light is represented by the following eqn (eqn (14)–(17)).[104]

$$BaSnO_3 + h\nu \rightarrow e^- + h^+ \quad (14)$$

$$e^- + O_2 \rightarrow O_2^{\cdot-} \quad (15)$$

$$h^+ + \mathbf{TC} \rightarrow \text{degradation} \quad (16)$$

$$O_2^{\cdot-} + \mathbf{TC} \rightarrow \text{degraded } \mathbf{TC} \text{ products} \quad (17)$$

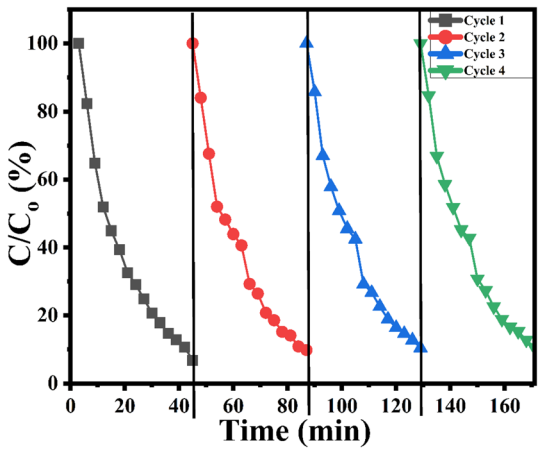

Fig. 13 Recyclability test of BSO photocatalyst, experimental conditions: [TC] = 0.01 g L^{-1}, BSO = 0.4 g L^{-1}, and volume: 80 ml.

3.3 Recyclability and stability studies

The reusability studies of the BSO were studied (Fig. 13). BSO exhibited excellent stability in the reuse study. Importantly, in the fourth cycle, photocatalytic activity was found to be more than 94%. This slight reduction in the activity may be attributed to the loss of the photocatalyst during the washing step. Further, Fig. S2† shows the comparative XRD plots before and after antibiotic degradation. It was observed that there was no significant decrease in the crystallinity of BSO even after use four times. Additionally, ICP-OES analysis was carried out to evaluate the leaching of active components, and the results showed minimal leaching of Ba (0.18%) and Sn (0.1%), indicating excellent chemical stability. Therefore, the slight reduction in degradation efficiency (from 100% to 94%) is primarily attributed to minor catalyst loss during the washing and recovery steps, rather than any significant deactivation.

The FESEM image shows well-separated smooth-surface cubes even after the degradation experiments (Fig. S3c†). The elemental composition of BSO after **TC** degradation remains largely unchanged and the atomic percentage and weight percentage of the elements are mentioned in the inset of Fig. S3d.† This indicates the stability of BSO following degradation. After the degradation experiment, the TEM image of BSO was also obtained which revealed no morphological changes (Fig. S4a and b†) compared to the fresh BSO. Overall, these results highlight the stability and reusability of BSO.

3.4 Degradation byproducts and toxicity

Degradation byproducts **TC-1** and **TC-2** were formed due to the cleavage of ring II, with complete ring-opening reactions and bond-breaking reactions, yielding smaller molecular fragments, as shown in Scheme 1. The loss of the side chain amino group in ring IV (deamination) and the amide group in ring IV

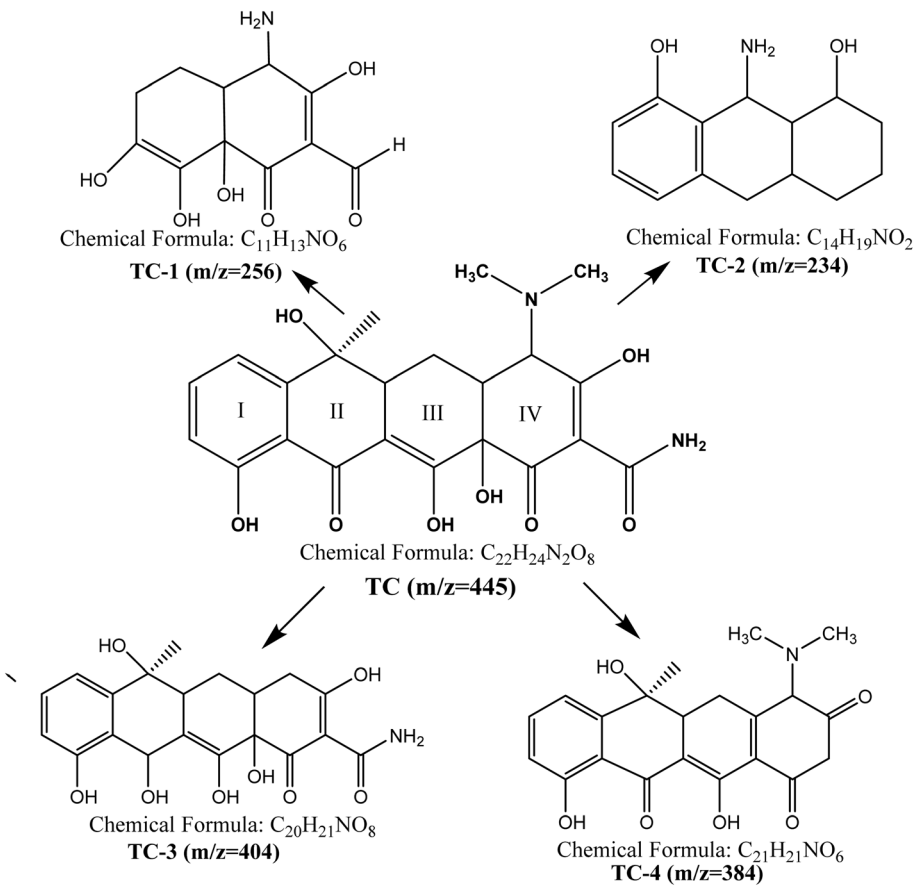

Scheme 1 Possible degradation mechanism of **TC** by BSO/UVA-LED system [TC] = 10 mg L^{-1}, BSO = 0.4 g L^{-1}, and volume: 80 ml.

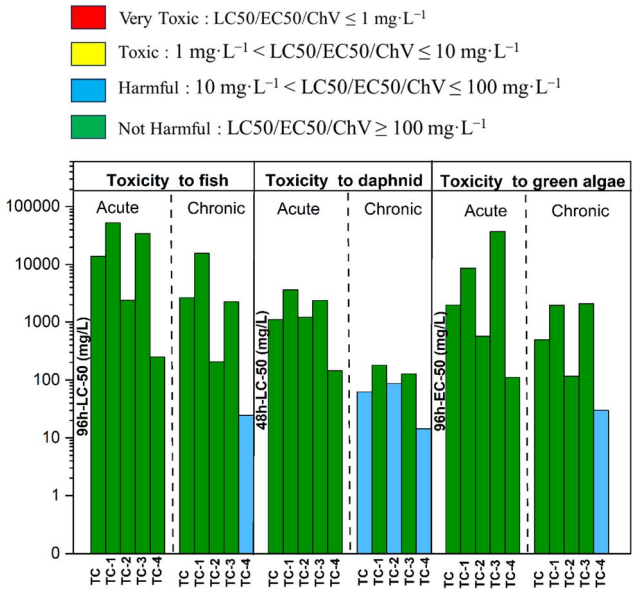

Fig. 14 ECOSAR analysis of TC and degradation byproduct of TC.

(deamidation) led to intermediate **TC-3** and **TC-4**, respectively (Fig. S11 and S12†). Similar degradation byproducts were earlier reported in photocatalysis.[105,106]

The ecotoxicity of **TC** and its degradation by-products using the ECOSAR model were presented in Fig. 14. **TC** and its degradation byproducts were predicted to be not harmful to acute toxicity towards fish, daphnids (LC50 value > 100 mg L^{-1}), and green algae (EC50 value >100 mg L^{-1}). Notably, **TC** and **TC-2** showed chronic toxicity against daphnids (categorised as harmful). **TC-4** was predicted chronic toxicity towards fish, daphnids, and green algae (categorised as harmful). Importantly, none of the by-products were predicted as being in the toxic chemical category, revealing the BSO/LED system as a potential system for treating **TC** without generating very toxic degradation byproducts (Fig. 14).[107]

3.5 Antibacterial activity assay

The antibacterial activity of **TC** before and after BSO/LED treatment (at 0–50 min) by BSO photocatalyst was determined (Fig. 15). These results reveal that **TC** (0.01 g L^{-1}) before treatment showed a zone of inhibition against target *E. faecalis* and *E. coli* (Fig. 15A and C). Notably, after treatment (50 min), degraded **TC** showed no zone of inhibition against *E. faecalis* and *E. coli.* Notably, BSO photocatalysts showed no antibacterial activity against *E. faecalis* and *E. coli* (Fig. 15A and C). These results reveal that treatment by the BSO/LED system caused the complete is first to demonstrate the degradation of **TC** by BSO/

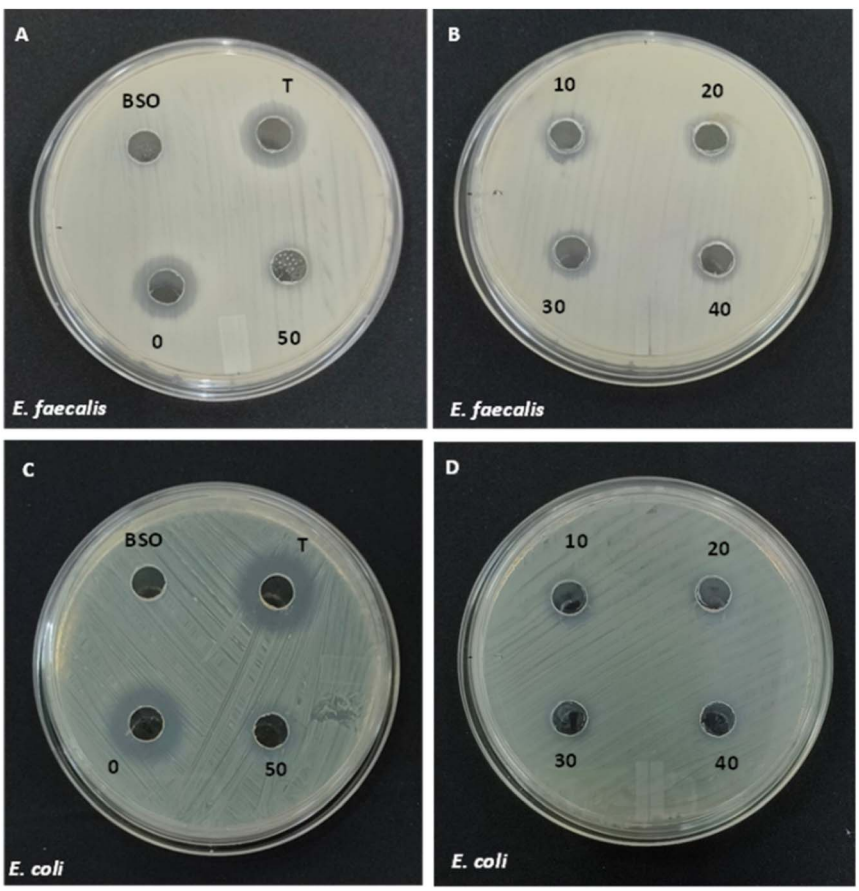

Fig. 15 Anti-bacterial activity of TC and of the treated solution withdrawn at time interval 0, 10, 20, 30, 40, and 50 min against *E. faecalis*, (A and B). Anti-bacterial activity of TC and of the treated solution withdrawn at time intervals 0, 10, 20, 30, 40, and 50 min against *E. coli* (C and D).

LED system with complete removal of the antibacterial activity of **TC**.[108] To the best of our knowledge, the present study of antibacterial activity is important to prevent the emergence of ARBs.

4. Conclusion

TC was effectively degraded by the proposed BSO/LED system. XRD revealed the cubic phase of BSO. FESEM revealed the cubic morphology of BSO. TEM image showed the aggregation of nanosheets of BSO to form a cubic block-like morphology. The BET analysis reveals the slit-like mesopores in BSO. XPS analysis confirmed the presence of Ba^{2+}, Sn^{4+} and lattice oxygen and adsorbed hydroxy species in BSO. At the optimised condition (BSO = 0.4 g L^{-1}, **TC** = 10 mg L^{-1}), the pseudo-first-order rate constant for **TC** degradation by the BSO/LED system was determined to be 0.0824 min^{-1}. The effects of the initial concentration of **TC**, dosage of BSO, and pH on **TC** degradation by the BSO/LED system were presented. The positive Mott–Schottky curve reveals that BSO is an n-type semiconductor with a flat band potential (E_{fb}) of −1.75 V (Vs Ag/AgCl). The radical scavenging results highlight the major role of superoxide ($O_2^{-\cdot}$) and holes (h^+) in the degradation of **TC**. ESR results confirmed the $O_2^{-\cdot}$ and h^+ were present in the BSO/LED system. The photocurrent experiments revealed the interaction of holes (h^+) with **TC**, thereby increasing the photocurrent compared to BSO. The antibacterial activity of **TC** against Gram-negative *Escherichia coli* (*E. coli*) and Gram-positive *Enterococcus faecalis* (*E. faecalis*) was completely lost after BSO/LED treatment. The degradation pathways involved ring opening, deamination and deamidation reactions to produce degradation byproducts, which were identified by high-resolution mass spectrometry. Importantly, ECOSAR analysis predicted these degradation byproducts to be non-toxic. Further, EE_o values were determined to be 13.63 kWh per m^3 per order, and the cost was estimated to be \$ 1 m^{-3}, revealing that the BSO/LED system is energy-efficient and cost-effective in removing **TC**. Overall, the finding presents the degradation of **TC** by the proposed stable and energy-efficient BSO/LED system with antibacterial activity removal which is important to prevent the spreading of ARBs.

Data availability

The data supporting this article have been included as part of the ESI.†

Conflicts of interest

There is no conflict to declare.

Acknowledgements

The authors acknowledge BITS Pilani, KK Birla Goa Campus for the PhD scholarship, and financial assistance for this research effort. Furthermore, author express thanks to the Department of Chemistry at BITS Pilani, KK Birla Goa Campus, provided access to BET, EIS, and UV-visible spectroscopy analysis, LC-MS, CSIF at BITS Pilani, KK Birla Goa Campus, provided FESEM, XRD, and Raman facilities. XPS was performed at CAL, BITS Pilani, Hyderabad Campus. The authors also acknowledge the Anusandhan National Research Foundation (ANRF- formerly DST-SERB) for a recently completed project that provided a desktop server for small-scale computations. Furthermore, the authors also acknowledge the Indian Institute of Technology, Bombay (IIT Bombay), India, for providing access to the ESR facilities and the University of Hyderabad for the TEM analysis.

References

1 M. Patel, R. Kumar, K. Kishor, T. Mlsna, C. U. Pittman and D. Mohan, Pharmaceuticals of emerging concern in aquatic systems: Chemistry, occurrence, effects, and removal methods, *Chem. Rev.*, 2019, **119**(6), 3510–3673.
2 D. O'Flynn, J. Lawler, A. Yusuf, A. Parle-Mcdermott, D. Harold, T. Mc Cloughlin, L. Holland, F. Regan and B. White, A review of pharmaceutical occurrence and pathways in the aquatic environment in the context of a changing climate and the COVID-19 pandemic, *RSC Adv.*, 2021, **5**, 575–594.
3 O. A. H. Jones, N. Voulvoulis and J. N. Lester, Human Pharmaceuticals in Wastewater Treatment Processes, *Crit. Rev. Environ. Sci. Technol.*, 2005, **35**(4), 401–427.
4 K. Samal, S. Mahapatra and M. Hibzur Ali, Pharmaceutical wastewater as Emerging Contaminants (EC): Treatment technologies, impact on environment and human health, *Energy Nexus*, 2022, **6**, 100076.
5 N. Kemper, Veterinary antibiotics in the aquatic and terrestrial environment, *Ecol. Indic.*, 2008, **8**(1), 1–13.
6 S. M. Zainab, M. Junaid, N. Xu and R. N. Malik, Antibiotics and antibiotic-resistant genes (ARGs) in groundwater: A global review on dissemination, sources, interactions, environmental and human health risks, *Water Res.*, 2020, **187**, 116455.
7 K. O'Malley, W. McDonald and P. McNamara, Antibiotic resistance in urban stormwater: a review of the dissemination of resistance elements, their impact, and management opportunities, *RSC Adv.*, 2023, **9**, 2188–2212.
8 L. T. Le, Z. Huang, K. Whiteson and S. Jiang, Water Impact Statement The Occurrence and Diversity of Antibiotic Resistance and Virulence Factor Genes in Wastewater from Four North American Treatment Plants, *RSC Adv.*, 2022, **8**, 1650–1664.
9 E. Y. Klein, I. Impalli, S. Poleon, P. Denoel, M. Cipriano, T. P. Van Boeckel, S. Pecetta, D. E. Bloom and A. Nandi, Global trends in antibiotic consumption during 2016–2023 and future projections through 2030, *Proc. Natl. Acad. Sci. U. S. A.*, 2024, **121**(49), e2411919121.
10 P. Suyana, P. Ganguly, B. N. Nair, S. C. Pillai and U. S. Hareesh, Structural and compositional tuning in g-C3N4 based systems for photocatalytic antibiotic degradation, *Chem. Eng. J. Adv.*, 2021, **8**, 100148.
11 I. Chopra and M. Roberts, Tetracycline Antibiotics: Mode of Action, Applications, Molecular Biology, and Epidemiology

of Bacterial Resistance, *Microbiol. Mol. Biol. Rev.*, 2001, **65**, 232–260.

12 D. Dionysiou, L. Puma, J. Ye, J. Schneider, D. Bahnemann, M. G. Antoniou, C. Zhao, K. E. O'shea, G. Zhang, D. D. Dionysiou, C. Zhao, C. Han, M. N. Nadagouda G, H. Choi, T. Fotiou, M. Triantis and A. Hiskia, Photocatalytic Degradation of Organic Contaminants in Water: Process Optimization and Degradation Pathways, *RSC Energy Environ. Ser.*, 2016, **15**, 1–34.

13 L. Xu, H. Zhang, P. Xiong, Q. Zhu, C. Liao and G. Jiang, Occurrence, fate, and risk assessment of typical tetracycline antibiotics in the aquatic environment: A Review, *Sci. Total Environ.*, 2021, **753**, 141975.

14 Y. Amangelsin, Y. Semenova, M. Dadar, M. Aljofan and G. Bjørklund, The Impact of Tetracycline Pollution on the Aquatic Environment and Removal Strategies, *Antibiotics*, 2023, **12**, 440.

15 Y. Liu, X. He, X. Duan, Y. Fu and D. D. Dionysiou, Photochemical degradation of oxytetracycline: Influence of pH and role of carbonate radical, *Chem. Eng. J.*, 2015, **276**, 113–121.

16 Y. Zhao, Z. Liu, L. Li, S. Jiang and C. Shi, Systematic review of randomized controlled trials of traditional Chinese medicine treatment of non-acute bronchial asthma complicated by gastroesophageal reflux, *J. Tradit. Chin. Med.*, 2012, **32**(1), 12–18.

17 H. Sah, Degradation patterns of tetracycline antibiotics in reverse micelles and water, *Biomed, Chromatogr.*, 2006, **20**(11), 1142–1149.

18 Y. Lin, S. Xu and J. Li, Fast and highly efficient tetracycline removal from environmental waters by graphene oxide functionalized magnetic particles, *Chem. Eng. J.*, 2013, **225**, 679–685.

19 A. Onal, Overview on liquid chromatographic analysis of tetracycline residues in food matrices, *Food Chem.*, 2011, **127**(1), 197–203.

20 M. H. Khan, H. Bae and J. Y. Jung, Tetracycline degradation by ozonation in the aqueous phase: Proposed degradation intermediates and pathway, *J. Hazard. Mater.*, 2010, **181**, 659–665.

21 Y. Ding, W. Jiang, B. Liang, J. Han, H. Cheng, M. R. Haider, H. Wang, W. Liu, S. Liu and A. Wang, UV photolysis as an efficient pretreatment method for antibiotics decomposition and their antibacterial activity elimination, *J. Hazard. Mater.*, 2020, **392**, 122321.

22 K. Sharma, A. Sudhaik, Sonu, R. Kumar, V. H. Nguyen, Q. Van Le, T. Ahamad, S. Thakur, S. Kaya, L. H. Nguyen, P. Raizada and P. Singh, Advanced photo-Fenton assisted degradation of tetracycline antibiotics using α-Fe_2O_3/CdS/SiO_2 based S-scheme photocatalyst, *J. Water Proc. Eng.*, 2024, **59**, 105011.

23 Y. Liu, H. Liu, Z. Zhou, T. Wang, C. N. Ong and C. D. Vecitis, Degradation of the Common Aqueous Antibiotic Tetracycline using a Carbon Nanotube Electrochemical Filter, *Environ. Sci. Technol.*, 2015, **49**, 7974–7980.

24 K. Wei, Y. Faraj, G. Yao, R. Xie and B. Lai, Strategies for improving perovskite photocatalysts reactivity for organic pollutants degradation: A review on recent progress, *Chem. Eng. J.*, 2021, **414**, 128783.

25 P. Swaminaathan, A. Saravanan, P. R. Yaashikaa and A. S. Vickram, Recent advances in photocatalytic degradation of persistent organic pollutants: Mechanisms, challenges, and modification strategies, *SCENV*, 2024, **8**, 100171.

26 Z. Yang, H. S. Xie, W. Y. Lin, Y. W. Chen, D. Teng and X. S. Cong, Enhanced Adsorption-Photocatalytic Degradation of Organic Pollutants *via* a ZIF-67-Derived Co-N Codoped Carbon Matrix Catalyst, *ACS Omega*, 2022, **7**(45), 40882–40891.

27 S. Li, C. Zhang, F. Li, T. Hua, Q. Zhou and S. H. Ho, Technologies towards antibiotic resistance genes (ARGs) removal from aquatic environment: A critical review, *J. Hazard. Mater.*, 2021, **411**(6), 125148.

28 X. Hu, X. Hu, Q. Peng, L. Zhou, X. Tan, L. Jiang, C. Tang, H. Wang, S. Liu, Y. Wang and Z. Ning, Mechanisms underlying the photocatalytic degradation pathway of ciprofloxacin with heterogeneous TiO_2, *Chem. Eng. J.*, 2020, **380**, 122366.

29 L. G. Raikar, A. Patel, J. Gandhi, K. V. K. Gupta and H. Prakash, Nano-TiO_2 immobilized polyvinylidene fluoride based spongy-spheres for ciprofloxacin photocatalytic degradation: antibacterial activity removal, mechanisms, UVA LED irradiation and easy recovery, *Environ. Sci. Nano.*, 2024, **9**, 3729–3743.

30 K. Wang, G. Zhang, J. Li, Y. Li and X. Wu, 0D/2D Z-Scheme Heterojunctions of Bismuth Tantalate Quantum Dots/Ultrathin g-C_3N_4 Nanosheets for Highly Efficient Visible Light Photocatalytic Degradation of Antibiotics, *ACS Appl. Mater. Interfaces*, 2017, **9**(50), 43704–43715.

31 N. Lin, Y. Gong, R. Wang, Y. Wang and X. Zhang, Critical review of perovskite-based materials in advanced oxidation system for wastewater treatment: Design, applications and mechanisms, *J. Hazard. Mater.*, 2022, **424**, 127637.

32 J. Wu, J. Chen, J. Gao, Z. Chen, L. Li and W. Wang, Recent Progress and Perspectives on Nonlead Halide Perovskites in Photocatalytic Applications, *Energy Fuels*, 2022, **36**(24), 14613–14624.

33 T. Tabari, H. Tavakkoli, P. Zargaran and D. Beiknejad, Fabrication of Perovskite-type Oxide $BaPbO_3$ Nanoparticles and their Efficiency in Photodegradation of Methylene Blue, *S. Afr. J. Chem.*, 2012, **65**, 239–244.

34 J. Li, H. L. Cao, W. Bin Jiao, Q. Wang, M. Wei, I. Cantone, J. Lü and A. Abate, Biological impact of lead from halide perovskites reveals the risk of introducing a safe threshold, *Nat. Commun.*, 2020, **11**, 310.

35 X. Chen, Q. Dong, S. Chen, Z. Zhang, X. Zhang, Y. Di, A. Jiang, D. Zhang and T. Li, Halloysite nanotubes supported BiVO4/BaSnO3 p–n heterojunction photocatalysts for the enhanced degradation of methylene blue under visible light, *Colloids Surf., A*, 2023, **664**, 131143.

36 S. Bimli, S. R. Mulani, E. Choudhary, V. Manjunath, P. Shinde, S. R. Jadkar and R. S. Devan, Perovskite $BaSnO_3$ nanoparticles for solar-driven bi-functional

photocatalytic activity: PEC water splitting and Wastewater treatment, *Int. J. Hydrogen Energy*, 2024, **51**, 1497–1507.

37 Z. M. Wong, H. Cheng, S. W. Yang, T. L. Tan and G. Q. Xu, Computational Design of Perovskite $Ba_xSr_{1-x}SnO_3$ Alloys as Transparent Conductors and Photocatalysts, *J. Phys. Chem. C*, 2017, **121**(47), 26446–26456.

38 A. S. Deepa, S. Vidya, P. C. Manu, S. Solomon, A. John and J. K. Thomas, Structural and optical characterization of $BaSnO_3$ nanopowder synthesized through a novel combustion technique, *J. Alloys Compd.*, 2011, **509**(5), 1830–1835.

39 S. Tao, F. Gao, X. Liu and O. T. Sùrensen, Ethanol-sensing characteristics of barium stannate prepared by chemical precipitation, *Sens. Actuators, B*, 2000, **71**(3), 223–227.

40 Y. H. Ochoa-Muñoz, J. E. Rodríguez-Páez and R. Mejía de Gutiérrez, Structural and optical study of perovskite nanoparticles $MSnO_3$ (M = Ba, Zn, Ca) obtained by a wet chemical route, *Mater. Chem. Phys.*, 2021, **266**, 124557.

41 A. Stanulis, S. Sakirzanovas, M. Van Bael and A. Kareiva, Sol-gel (combustion) synthesis and characterization of different alkaline earth metal (Ca, Sr, Ba) stannates, *J. Sol-Gel Sci. Technol.*, 2012, **64**(3), 643–652.

42 M. Licheron, G. Jouarf and E. Hussona, Characterization of $BaSnO_3$, Powder Obtained by a Modified Sol-Gel Route, *J. Eur. Ceram. Soc.*, 1997, **17**, 1453–1457.

43 K. Habeeba, T. E. Manjulavalli, D. V. Ezhilarasi Gnanakumari and V. Karthikadevi, Highly crystalline perovskite $BaSnO_3$ nanopowder synthesised using hydrothermal technique, *Mater. Res. Express*, 2019, **6**(9), 094004.

44 N. Bader and B. Zimmermann, Co-precipitation as a sample preparation technique for trace element analysis: An overview, *Int. J. Chem. Sci.*, 2014, **12**(2), 519–525.

45 Y. Jayavelu, G. Maharana, G. Rajender, R. Muniramaiah, S. Divyadharshini, B. H. Baby, M. Kovendhan, J. M. Fernandes and D. P. Joseph, Defect-mediated time-efficient photocatalytic degradation of methylene blue and ciprofloxacin using tungsten-incorporated ternary perovskite BaSnO3 nanoparticles, *Chemosphere*, 2024, **351**, 141128.

46 X. Zhu, F. Qin, Y. Luo, L. Zhang, D. Yang, W. Feng and S. Chen, Enhanced photocatalytic activity of p ($BaSnO_3$)-n (anatase/rutile/brookite TiO_2) heterojunction composites by efficient interfacial charge transfer, *J. Mol. Struct.*, 2023, **1294**, 136440.

47 T. Li, A. Jiang, Y. Di, D. Zhang, X. Zhu, L. Deng, X. Ding and S. Chen, Novel $BaSnO_3/TiO_2$ @HNTs Heterojunction Composites with Highly Enhanced Photocatalytic Activity and Stability, *ChemistrySelect*, 2021, **6**(40), 10817–10826.

48 J. E. Yager and C. David Yue, Environmental Chemistry Evaluation of the Xenon Arc Lamp As A Light Source For Aquatic Photodegradation Studies: Comparison With Natural Sunlight, *Environ. Chem.*, 1988, **7**(12), 1003–1011.

49 W. Aggoune, A. Eljarrat, D. Nabok, K. Irmscher, M. Zupancic, Z. Galazka, M. Albrecht, C. Koch and C. Draxl, A consistent picture of excitations in cubic $BaSnO_3$ revealed by combining theory and experiment, *Commun. Mater.*, 2022, **3**(1), 12.

50 M. Asisi Janifer, S. Anand, C. Joseph Prabagar and S. Pauline, Structural and optical properties of $BaSnO_3$ ceramics by solid state reaction method, *Mater. Today Proc.*, 2021, **47**, 2067–2070.

51 I. A. Mkhalid and S. I. El-Hout, S-scheme $AgVO_3$-decorated $BaSnO_3$ heterojunction for efficient photoreduction of Mercury (II) ions under visible light, *J. Taiwan Inst. Chem. Eng.*, 2023, **146**, 104896.

52 X. Song, W. Jiang, Z. Cai, X. Yue, X. Chen, W. Dai and X. Fu, Visible light-driven deep oxidation of NO and its durability over Fe doped $BaSnO_3$: The NO^+ intermediates mechanism and the storage capacity of Ba ions, *Chem. Eng. J.*, 2022, **444**, 136709.

53 K. A. Alzahrani and A. A. Ismail, Enhanced photocatalytic performances of highly efficient perovskite $BaSnO_3$ nanorods decorated by $CuMn_2O_4$ nanoparticles, *J. Photochem. Photobiol., A*, 2023, **435**, 114298.

54 M. Figueredo, E. M. Rodríguez, E. M. Cordero and F. J. Beltrán, UVA LEDs and solar light photocatalytic oxidation/ozonation as a tertiary treatment using supported TiO2: With an eye on the photochemical properties of the secondary effluent, *J. Environ. Chem. Eng.*, 2022, **10**(2), 107371.

55 C. Langford, M. Izadifard, E. Radwan and G. Achari, Some observations on the development of superior photocatalytic systems for application to water purification by the "Adsorb and shuttle" or the interphase charge transfer mechanisms, *Molecules*, 2014, **19**, 19557–19572.

56 W. K. Jo and R. J. Tayade, New Generation Energy-Efficient Light Source for Photocatalysis: LEDs for Environmental Applications, *Ind. Eng. Chem. Res.*, 2014, **53**, 2073–2084.

57 M. Forouzandeh-Malati, F. Ganjali, E. Zamiri, S. Zarei-Shokat, F. Jalali, M. Padervand, R. Taheri-Ledari and A. Maleki, Efficient Photodegradation of Eriochrome Black-T by a Trimetallic Magnetic Self-Synthesized Nanophotocatalyst Based on Zn/Au/Fe-Embedded Poly(vinyl alcohol), *Langmuir*, 2022, **38**, 13728–13743.

58 S. Sharma, R. Shanmugam, R. B. Harikrishna, U. Prasad, G. Ranga Rao and A. M. Kannan, Y_2O_3 electrodeposited TiO_2 nanotube arrays as photoanode for enhanced photoelectrochemical water splitting, *Int. J. Hydrogen Energy*, 2024, **52**, 1415–1427.

59 C. Zhang, L. Chen, H. Luo, H. Weng, F. Qin, D. Qin and D. Huang, Selective micropollutants removal in wastewaters by non-radical activation of peroxymonosulfate: Multiparameter analysis of electron-donating capacity, *Appl. Catal. B Environ.*, 2025, **362**, 124695.

60 L. G. Raikar, J. Gandhi, K. V. K. Gupta and H. Prakash, Degradation of Ampicillin with antibiotic activity removal using persulfate and submersible UVC LED: Kinetics, mechanism, electrical energy and cost analysis, *Chemosphere*, 2023, **349**, 140831.

61 X. Zhang, M. Feng, R. Qu, H. Liu, L. Wang and Z. Wang, Catalytic degradation of diethyl phthalate in aqueous solution by persulfate activated with nano-scaled magnetic $CuFe_2O_4$/MWCNTs, *Chem. Eng. J.*, 2016, **301**, 1–11.

62 A. A. Ioannidi, G. Bampos, M. Antonopoulou, P. Oulego, G. Boczkaj, D. Mantzavinos and Z. Frontistis, Sonocatalytic degradation of Bisphenol A from aquatic matrices over Pd/CeO2 nanoparticles: Kinetics study, transformation products, and toxicity, *Sci. Total Environ.*, 2024, 919.

63 J. H. Jorgensen and M. J. Ferraro, Antimicrobial Susceptibility Testing: A Review of General Principles and Contemporary Practices, *Clin. Infect. Dis.*, 2009, **49**, 1749–1755.

64 J. Farkas, M. Náfrádi, T. Hlogyik, B. Cora Pravda, K. Schrantz, K. Hernádi and T. Alapi, Comparison of advanced oxidation processes in the decomposition of diuron and monuron-efficiency, intermediates, electrical energy per order and the effect of various matrices, *Environ. Sci.*, 2018, **4**, 1345–1360.

65 U. Kumar, M. J. Ansaree and S. Upadhyay, Structural and optical characterizations of $BaSnO_3$ nanopowder synthesized by aqueous sol-gel method, *Process. Appl. Ceram.*, 2017, **11**(3), 177–184.

66 K. Momma and F. Izumi, VESTA 3 for three-dimensional visualization of crystal, volumetric and morphology data, *J. Appl. Crystallogr.*, 2011, **44**, 1272–1276.

67 K. R. Dileep, M. K. Rajbhar, A. Ashina, E. Ramasamy, S. Mallick, T. N. Rao and G. Veerappan, A facile co-precipitation method for synthesis of Zn doped $BaSnO_3$ nanoparticles for photovoltaic application, *Mater. Chem. Phys.*, 2021, **258**, 123939.

68 T. N. Stanislavchuk, A. A. Sirenko, A. P. Litvinchuk, X. Luo and S. W. Cheong, Electronic band structure and optical phonons of $BaSnO_3$ and $Ba_{0.97}La_{0.03}SnO_3$ single crystals: Theory and experiment, *J. Appl. Physiol.*, 2012, **112**(4), 044108.

69 N. Rajamanickam, K. Jayakumar and K. Ramachandran, Effect of iron doping on magnetic and electrical properties of $BaSnO_3$ nanostructures, *J. Mater. Sci.: Mater. Electron.*, 2018, **29**, 19880–19888.

70 J. John, M. Dhananjaya, S. Suresh, S. Savitha Pillai, M. Sahoo, O. M. Hussain, R. Philip and V. P. Mahadevan Pillai, Effect of manganese doping on the structural, morphological, optical, electrical, and magnetic properties of $BaSnO_3$, *J. Mater. Sci.: Mater. Electron.*, 2020, **31**, 11159–11176.

71 J. John, S. Suresh, S. Pillai.S, R. Philip and V. P. M. Pillai, Effect of Fe doping on the structural, morphological, optical, magnetic and dielectric properties of $BaSnO_3$, *J. Mater. Sci.: Mater. Electron.*, 2021, **32**, 11763–11780.

72 M. Thommes, K. Kaneko, A. V. Neimark, J. P. Olivier, F. Rodriguez-Reinoso, J. Rouquerol and K. S. W. Sing, Physisorption of gases, with special reference to the evaluation of surface area and pore size distribution (IUPAC Technical Report), *Pure Appl. Chem.*, 2015, **87**, 1051–1069.

73 A. Marikutsa, M. Rumyantseva, A. Baranchikov and A. Gaskov, Nanocrystalline $BaSnO_3$ as an alternative gas sensor material: Surface reactivity and high sensitivity to SO_2, *Materials*, 2015, **8**, 6437–6454.

74 W. Zhang, F. A. Guo and G. Li, Barium staminate as semiconductor working electrodes for dye-sensitized solar cells, *Int. J. Photoenergy*, 2010, **2010**, 1–7.

75 A. Marikutsa, M. Rumyantseva, A. Baranchikov and A. Gaskov, Nanocrystalline $BaSnO_3$ as an Alternative Gas Sensor Material: Surface Reactivity and High Sensitivity to SO_2, *Materials*, 2015, **8**(9), 6437–6454.

76 J. John, S. Suresh, S. Savitha Pillai, R. Philip and V. P. Mahadevan Pillai, Structural, Morphological, Magnetic and Optical Limiting Performance of Ni Doped $BaSnO_3$, *J. Electron. Mater.*, 2021, **50**, 5868–5880.

77 L. H. Grey, H. Y. Nie and M. C. Biesinger, Defining the nature of adventitious carbon and improving its merit as a charge correction reference for XPS, *Appl. Surf. Sci.*, 2024, **653**, 159319.

78 S. H. Butt, M. S. Rafique, K. Siraj, A. Latif, A. Afzal, M. S. Awan, S. Bashir and N. Iqbal, Epitaxial thin-film growth of Ruddlesden–Popper-type $Ba_3Zr_2O_7$ from a $BaZrO_3$ target by pulsed laser deposition, *Appl. Phys. A:Mater. Sci. Process.*, 2016, **122**(7), 658.

79 J. John, S. R. Chalana, R. Prabhu and V. P. Mahadevan Pillai, Effect of oxygen pressure on the structural and optical properties of $BaSnO_3$ films prepared by pulsed laser deposition method, *Appl. Phys. A:Mater. Sci. Process.*, 2019, **125**(3), 155.

80 J. C. Dupin, D. Gonbeau, P. Vinatier and A. Levasseur, Systematic XPS studies of metal oxides, hydroxides and peroxides, *Phys. Chem. Chem. Phys.*, 2000, **2**, 1319–1324.

81 L. Q. Wu, Y. C. Li, S. Q. Li, Z. Z. Li, G. D. Tang, W. H. Qi, L. C. Xue, X. S. Ge and L. L. Ding, Method for estimating ionicities of oxides using O1s photoelectron spectra, *AIP Adv.*, 2015, **5**(9), 097210.

82 S. Gupta, J. Gandhi, S. Kokate, L. G. Raikar, V. G. Kopuri and H. Prakash, Augmented photocatalytic degradation of Acetaminophen using hydrothermally treated g-C_3N_4 and persulfate under LED irradiation, *Heliyon*, 2023, **9**, e16450.

83 S. Kokate, S. Gupta, V. G. Kopuri and H. Prakash, Energy efficient photocatalytic activation of peroxymonosulfate by g-C_3N_4 under 400 nm LED irradiation for degradation of Acid Orange 7, *Chemosphere*, 2022, **287**, 132099.

84 J. Wang, C. Liu, J. Feng, D. Cheng, C. Zhang, Y. Yao, Z. Gu, W. Hu, J. Wan and C. Yu, MOFs derived Co/Cu bimetallic nanoparticles embedded in graphitised carbon nanocubes as efficient Fenton catalysts, *J. Hazard. Mater.*, 2020, **394**, 122567.

85 M. Hasham Firooz, A. Naderi, M. Moradi and R. R. Kalantary, Enhanced tetracycline degradation with TiO_2/natural pyrite S-scheme photocatalyst, *Sci. Rep.*, 2024, **14**, 4954.

86 S. Sun, Y. Zhou, Y. Chen, Y. Wu and S. Bao, The performance and mechanism of phosphotungstic acid-modified NiFe-LDH heterogeneous photo-Fenton catalyst

for efficient degradation of tetracycline, *Environ. Sci.: Nano*, 2024, **11**, 4321–4336.

87 F. Saadati, N. Keramati and M. M. Ghazi, Influence of parameters on the photocatalytic degradation of tetracycline in wastewater: A review, *Crit. Rev. Environ. Sci. Technol.*, 2016, **46**, 757–782.

88 S. Wu, X. Li, Y. Tian, Y. Lin and Y. H. Hu, Excellent photocatalytic degradation of tetracycline over black anatase-TiO2 under visible light, *Chem. Eng. J.*, 2021, **406**, 126747.

89 C. Hu, H. Huang, F. Chen, Y. Zhang, H. Yu and T. Ma, Coupling Piezocatalysis and Photocatalysis in Bi_4NbO_8X (X = Cl, Br) Polar Single Crystals, *Adv. Funct. Mater.*, 2020, **30**, 1908168.

90 V. Vaiano, G. Iervolino and L. Rizzo, Cu-doped ZnO as efficient photocatalyst for the oxidation of arsenite to arsenate under visible light, *Appl. Catal. B Environ*, 2018, **238**, 471–479.

91 L. Xu, H. Zhang, P. Xiong, Q. Zhu, C. Liao and G. Jiang, Occurrence, fate, and risk assessment of typical tetracycline antibiotics in the aquatic environment: A review, *Sci. Total Environ.*, 2021, **753**, 141975.

92 J. Gandhi and H. Prakash, Photo-disinfection processes for bacterial inactivation and underlying principles for water constituents' impact: A review, *Chem. Eng. J. Adv.*, 2023, **14**, 100482.

93 N. Li, Y. Wang, X. Cheng, H. Dai, B. Yan, G. Chen, L. Hou and S. Wang, Influences and mechanisms of phosphate ions onto persulfate activation and organic degradation in water treatment: A review, *Water Res.*, 2022, **222**, 118896.

94 S. Li, C. Wang, Y. Liu, M. Cai, Y. Wang, H. Zhang, Y. Guo, W. Zhao, Z. Wang and X. Chen, Photocatalytic degradation of tetracycline antibiotic by a novel $Bi_2Sn_2O_7$/Bi_2MoO_6 S-scheme heterojunction: Performance, mechanism insight and toxicity assessment, *Chem. Eng. J.*, 2022, **429**, 132519.

95 C. Yin, Y. Liu, X. Kang and X. Li, Synergistic degradation of tetracycline by CDs decorated g-C_3N_4 under LED light irradiation combined with the persulfate-based advanced oxidation process, *Appl. Catal. A Gen.*, 2022, **636**, 118571.

96 H. Zhang, J. Joseph, C. Felix and B. Kalyanaraman, Bicarbonate Enhances the Hydroxylation, Nitration, and Peroxidation Reactions Catalyzed by Copper, Zinc Superoxide Dismutase Intermediacy Of Carbonate Anion Radical, *J. Biol. Chem.*, 2000, **275**, 14038–14045.

97 I. Milošević, S. Guillot, M. Tadić, M. Duttine, E. Duguet, K. Pierzchala, A. Sienkiewicz, L. Forró and M. L. Saboungi, Loading and release of internally self-assembled emulsions embedded in a magnetic hydrogel, *Appl. Phys. Lett.*, 2014, **104**, 043701.

98 D. Y. Xing, X. D. Zhao, C. S. He and B. Lai, Kinetic study and DFT calculation on the tetracycline abatement by peracetic acid, *Chin. Chem. Lett.*, 2024, **35**(9), 109436.

99 S. Bimli, S. R. Mulani, E. Choudhary, V. Manjunath, P. Shinde, S. R. Jadkar and R. S. Devan, Perovskite $BaSnO_3$ nanoparticles for solar-driven bi-functional photocatalytic activity: PEC water splitting and Wastewater treatment, *Int. J. Hydrog. Energy*, 2024, **51**, 1497–1507.

100 W. Zhang, L. Zhou, J. Shi and H. Deng, Synthesis of Ag3PO4/G-C3N4 Composite with Enhanced Photocatalytic Performance for the Photodegradation of Diclofenac under Visible Light Irradiation, *Catalysts*, 2018, **8**, 45.

101 C. Hu, H. Huang, F. Chen, Y. Zhang, H. Yu and T. Ma, Coupling Piezocatalysis and Photocatalysis in Bi_4NbO_8X (X = Cl, Br) Polar Single Crystals, *Adv. Funct. Mater.*, 2020, **30**, 1908168.

102 R. Yanagi, T. Zhao, D. Solanki, Z. Pan and S. Hu, Charge Separation in Photocatalysts: Mechanisms, Physical Parameters, and Design Principles, *ACS Energy Lett.*, 2022, **7**, 432–452.

103 J. Ni, W. Wang, D. Liu, Q. Zhu, J. Jia, J. Tian, Z. Li, X. Wang and Z. Xing, Oxygen vacancy-mediated sandwich-structural TiO_{2-x}/ultrathin g-C_3N_4/TiO_{2-x} direct Z-scheme heterojunction visible-light-driven photocatalyst for efficient removal of high toxic tetracycline antibiotics, *J. Hazard. Mater.*, 2021, **408**, 124432.

104 A. A. Baoum and A. A. Ismail, Enhanced photocatalytic efficiency of highly effective and stable perovskite $BaSnO_3$ with monoclinic Li_2MnO_3 nanoparticles: Atrazine a case study of herbicide, *Ceram. Int.*, 2023, **49**, 23227–23237.

105 X. Yu, X. Jin, M. Li, Y. Yu, M. Zhu, S. Tang, H. Zhou, K. Wang, R. Dou and J. Sun, Degradation mechanism of tetracycline using sulfidated nanoscale zerovalent iron driven peroxymonosulfate and metabolomic insights into environmental risk of intermediates products, *Chem. Eng. J.*, 2022, **430**, 133141.

106 Z. Maa, L. Hub, X. Lia, L. Denga, G. Fana and Y. Heb, A novel nano-sized MoS_2 decorated Bi_2O_3 heterojunction with enhanced photocatalytic performance for methylene blue and tetracycline degradation, *Ceram. Int.*, 2019, **45**, 15824–15833.

107 H. Liu, J. Qu, T. Zhang, M. Ren, Z. Zhang, F. Cheng, D. He and Y. nan Zhang, Insights into degradation pathways and toxicity changes during electro-catalytic degradation of tetracycline hydrochloride, *Environ. Pollut.*, 2019, **258**, 113702.

108 A. Patidar, V. R. Dugyala, S. Chakma, M. N. Galodiya and A. S. Giri, Reactive oxygen species aided photocatalytic degradation of tetracycline using non-metal activated carbon doped TiO_2 nanocomposite under UV-light irradiation, *Res. Chem. Intermed.*, 2024, **50**, 1035–1063.